



## A new gust parameterization for weather prediction models

Alejandro Gutiérrez<sup>a,\*</sup>, Robert G. Fovell<sup>b</sup>

<sup>a</sup> Instituto de Mecánica de los Fluidos e Ingeniería Ambiental, Facultad de Ingeniería, Universidad de la República, Montevideo, Uruguay

<sup>b</sup> Atmospheric and Environmental Sciences, University at Albany, State University of New York, United States

### ARTICLE INFO

**Keywords:**  
Wind energy  
Forecast  
Gust

### ABSTRACT

We analyze Uruguayan measurements, focusing on gusts at turbine hub height. Large gusts, exceeding 15 m/s, are observed to occur when the surface layer (as assessed by the bulk Richardson number  $Ri$ ) is neutral, and are uncommon when the layer is stable or even unstable. Gust factors (the ratio of the gusts to the mean winds) are inversely related to the mean winds but increase as the atmosphere becomes more unstable. Numerical simulations using different planetary boundary layer (PBL) schemes and mesoscale grid resolutions are employed in the development of a gust parameterization (GP) utilizing forecasts of surface layer  $Ri$  and winds above hub height. The GP, which provides gust factors to be applied to predicted turbine-level winds, provides higher skill at relatively coarser resolution than a simpler algorithm based solely on surface layer information, although its success is strongly dependent on the PBL and surface layer schemes selected.

### 1. Introduction

Wind gusts represent the maximum wind speed observed over a fixed period (WMO, 2018), and reliable gust forecasts can potentially mitigate the destruction and human losses they can cause (Friederichs et al., 2009). Gusts are particularly relevant to engineering applications such as wind energy production, especially in systems such as Uruguay's, which has a wind power participation of 35% (UTE, 2017). Gusts can cause equipment failures and pose danger to human life during maintenance activities. Additionally, commercial wind turbines typically have model-dependent cut-out velocities between 15 and 25 m/s, and when this threshold is reached, the machine abruptly stops (Barros, 2011). Thus, cut-out events pose a risk because they cause transitory changes in power transmission in electric lines (Hansen et al., 2010). Furthermore, as wind gusts can occur over synoptic or mesoscale time and length scales, the entire electric grid of a small nation like Uruguay can be at risk when extreme wind gusts occur, which would in turn affect electricity supply. As a consequence, the development of a skillful wind and gust forecasting model can help in electrical system management.

Wind energy is harvested at the lowest region of the planetary boundary layer (PBL), the region of the atmosphere that is directly affected by exchanges of momentum, heat, and mass with the surface and where diurnal variations are significant. Turbine blades in onshore wind farms sweep through areas between 60 and 120 m above ground level

(AGL), which includes the portion of the PBL known as the surface layer (SL) (Monin and Obukhov, 1954). Stability in this region of the atmosphere is particularly relevant to gust analysis (Wieringa, 1973); explored the relationship among gusts, friction velocities, the variation of measurements, and vertical stability. During the day, a convective mixed layer driven by buoyant plumes is typically found above the SL, perhaps reaching a depth of 1–2 km by mid-afternoon. Around sunset, a rapid decrease in turbulent motion in the boundary layer occurs as the SL stabilizes and the buoyant plumes that maintain the motion lose their energy source near the surface (Acevedo and Fitzjarrald, 2001). As a consequence, the diurnal cycle of solar radiation determines the stability of the PBL.

While wind gusts can be produced by convective systems such as thunderstorms and downbursts (cf., Choi and Hidayat, 2002; Shu et al., 2015), and other synoptic and mesoscale phenomena (e.g., Letson et al., 2018), the energy-containing turbulent eddies themselves are usually far too small to resolve in mesoscale numerical models (Wyngaard, 2004). As a consequence, when mesoscale models are used, gusts must be parameterized in some fashion, just as the PBL and surface layer must be. This is tricky because for practical reasons, operational models may need to employ horizontal resolutions that reside within the so-called gray zone (Wyngaard, 2004), in which turbulence is only partially resolved. Also, it may be necessary to handle convective and non-convective gusts separately, as the former may have different characteristics and yet still

\* Corresponding author.

E-mail address: [aguti@fing.edu.uy](mailto:aguti@fing.edu.uy) (A. Gutiérrez).

URL: <http://www.fing.edu.uy>

<https://doi.org/10.1016/j.jweia.2018.04.005>

Received 30 December 2017; Received in revised form 5 April 2018; Accepted 7 April 2018

be a threat to wind power systems (e.g., Kwon et al., 2012).

Many wind speed and gust forecasting methods have been proposed and evaluated for a wide variety of locations, phenomena, and conditions (Sheridan, 2011). has summarized some parameterizations in use for non-convective and convective gusts. Some are directly based on physical processes, such as (Brasseur, 2001), which characterizes gusts as boundary layer parcels drawn downward to the surface (Goyette et al., 2003); evaluated that approach in a regional climate model. Others utilize friction velocity (the surface turbulent momentum flux; Panofsky et al., 1977) or even constant gust factors (the ratio of the gusts and mean winds; Stucki et al., 2016; Fovell and Cao, 2017; Cao and Fovell, 2018). Still others, such as (Patlakas et al., 2017) and (Friederichs et al., 2009), combine model forecasts or analyses with statistical methods. Regarding convective gusts (Gray, 2003), used an algorithm to predict the maximum gust utilizing cloud top height, cloud depth, and virtual potential temperature, while the (Nakamura et al., 1996) approach incorporated downdraft depth and precipitation mixing ratio.

In this paper, we explore using the Weather Research and Forecasting (WRF) model (Skamarock and co-authors, 2008) as a tool to identify wind gust occurrence and large gust magnitude, irrespective of origin, motivated by and verified against observations collected at towers maintained by the Uruguyan electric utility. The emphasis is on crafting skillful “gust alarms”, based on a relevant speed threshold and appropriate forecast time windows. This will necessarily depend on the mean wind simulations being of reasonable quality. Wind forecasts are potentially sensitive to a wide variety of model factors, including initialization, resolution, and parameterizations such as the PBL and land surface models (LSM) (e.g., Stucki et al., 2016; Siuta et al., 2017; Cao and Fovell, 2016, 2018). In particular (Stucki et al., 2016), reported that WRF tended to overpredict the mean wind, while (Cao and Fovell, 2016, 2018), which utilized a dense mesonet to verify winds and gust forecasts during “Santa Ana” windstorms, demonstrated that this can be LSM-dependent, owing to its specification of surface roughnesses.

A variety of horizontal resolutions, ranging from 12 to 0.444 km, are examined herein. The WRF model contains a large number of PBL and SL schemes, some based on estimating turbulent kinetic energy (TKE) and others utilizing non-local closures (such as (Hong et al., 2006)) or representing hybrid approaches (e.g., Pleim, 2007a; Pleim, 2007b). At least one non-local scheme (Shin and Hong, 2013, 2015) specifically addresses the gray zone issue by directly considering the horizontal grid scale. Information from the PBL and SL parameterizations will be used in the construction of a gust parameterization that will predict the appropriate gust factor to be applied to simulated mean winds at hub height (~100 m AGL). Our approach, which extends the work of (Gutiérrez and Fovell, 2015), will be compared to a simpler model for non-convective gusts based on (Panofsky et al., 1977) that has been used at ECMWF (ECMWF, 2015), but applied to sustained winds predicted at hub height rather than at 10 m AGL.

The structure of this paper is as follows we present: in Section 2, the observational data available in Uruguay are described, followed in Section 3 by an analysis of the observed diurnal cycle in gusts, gust factors, and stability parameters. Section 4 describes the WRF experiments, and sensitivity to horizontal grid spacing and PBL/SL treatment is discussed in Section 5, along with our proposed parameterization. The performance of that gust model and the ECMWF algorithm is assessed in Section 6. Conclusions are offered in Section 7.

## 2. Wind gusts: observational data

With a focus on developing a gust parameterization, we analyzed observational data recorded by the UTE (Administración Nacional de Usinas y Transmisiones Eléctricas) to assess wind energy resources. UTE installed a set of towers with anemometers, wind vanes, pyranometers, and thermometers throughout Uruguay, which is dominated by rolling plains and low mountain ranges with all elevations being < 500 m above mean sea level. The four towers are located in three distinct geographical

regions (Fig. 1). The first region is close to the La Plata River, including an estuary composed of seawater and freshwater from the Parana River and the Uruguay River, and is the site of the Rosendo Mendoza (RM) and Colonia Eulacio (CE) towers. The second region is close to the Atlantic Ocean, its tower being called Jose Ignacio (JI). The third region is further inland, at least 300 km from the La Plata River and the Atlantic Ocean, represented by the Aparicio Saravia (AS) tower.

The towers are equipped with two anemometers mounted orthogonally to filter the effect of the tower wake. The installation adhered to IEC standard 61400-12 (IEC, 1998). The wind measurements were performed with cup anemometers (NRG Systems 40, with a distance constant of 3 m) and wind vanes (NRG Systems 200P) mounted at various heights, including turbine level (approx. 100 m). Table 1 describes the measurements considered in this work. The time periods were selected based on the quality and completeness of the wind data. Gusts were determined from 2-s samples (0.5 Hz being the sampling frequency) and the mean winds averaged these samples over 10-min intervals.

## 3. Analysis of observational data

### 3.1. Diurnal variation

The analysis of the observational data in this section begins with a description of the mean diurnal cycle and seasonal variations of near-surface stability and wind gusts. The data analyzed consisted of periods of twelve consecutive months, representing 2012 or 2014–15 (see Table 1). To determine the diurnal cycles, hourly values were sampled from the 10-min data and then averaged within four conventionally-defined seasons (e.g., winter is June 21–September 20, etc.). Then, a more detailed analysis is given for significant gust events, the goal being to identify the dimensional and nondimensional parameters that could be helpful in the development of a wind gust parameterization.

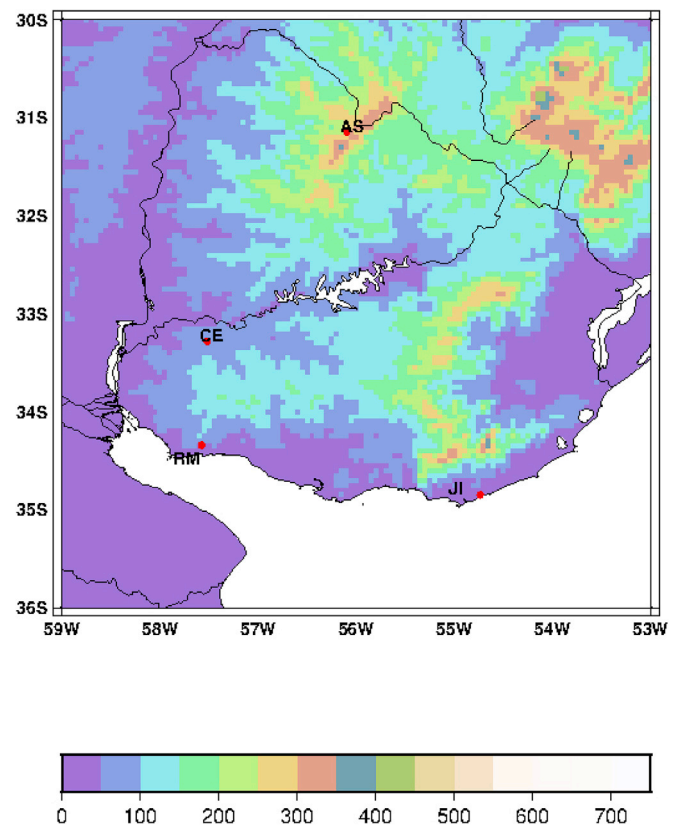


Fig. 1. Locations and topography (m) of towers from where observational data was measured.

**Table 1**

Tower locations, height of measurement considered, and period of analysis.

	Lat-S	Long-W	Top wind (m)	Bottom wind (m)	Top temp (m)	Bottom temp (m)	Time period
AS	31.143	56.095	101	–	99	5	01/01/2012–31/12/2012
CE	33.28	57.522	101.8	10.1	100.8	3.4	08/08/2014–07/08/2015
JI	34.85	54.735	98	12	98	12	01/01/2012–31/12/2012
RM	34.343	57.578	101	–	100	2	01/01/2012–31/12/2012, 08/08/2014–07/08/2015

Fig. 2 presents the diurnal cycle of the near-surface vertical temperature gradient ( $\frac{\partial T}{\partial z}$ ) for the four towers, computed using observations taken between 2–12 m and 98–101.8 m AGL, depending on the tower (Table 1). Larger (especially positive) values of the gradient indicate stability, while absolutely unstable (superadiabatic) conditions exist when  $\frac{\partial T}{\partial z} < -\Gamma_d$ , where  $\Gamma_d \approx 0.01$  °C/m is the dry adiabatic rate. After sunrise, superadiabatic temperature gradients were frequently observed in all seasons, consistent with prior observations (Takle, 1983; Czarnecki, 2012). Turbulent motions very near the ground are restricted, leaving insufficient vertical mixing to remove the absolute instability.

Some variations in the diurnal cycles in stability can be noted among these sites, reflecting their regional and local situations. Aparicio Saravia (AS) and Colonia Eulacio (CE) exhibited the largest degree of instability during the afternoon hours, consistent with their more inland locations (Fig. 1). The Jose Ignacio (JI) tower, located on the east coast near the ocean, was the least stable during the nighttime in all seasons, perhaps reflecting both local conditions and measurement details. An analysis of solar radiation (Abal et al., 2011) shows the east coast receives less radiation during the day, which is related to the higher incidence of cloud cover. If the cloudiness persists into the night, less nocturnal cooling and stability could be expected. Another difference is JI's lower thermometer is mounted at 12 m (see Table 1), higher than at Rosendo Mendoza (RM) and AS (2 and 5 m, respectively), so the nighttime inversion was also less well resolved.

The gust factor  $GF$  is defined as the ratio of the gust  $g$  and mean wind velocity  $\bar{V}$ :

$$GF = g/\bar{V}, \tag{1}$$

Both having been recorded at tower top (roughly 100 m; Table 1). The

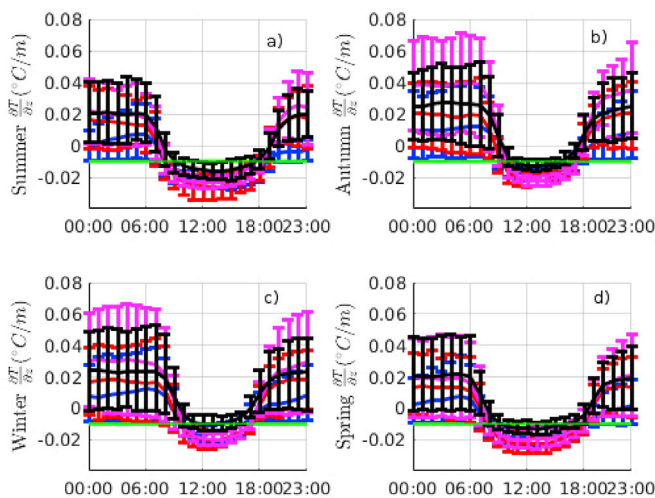


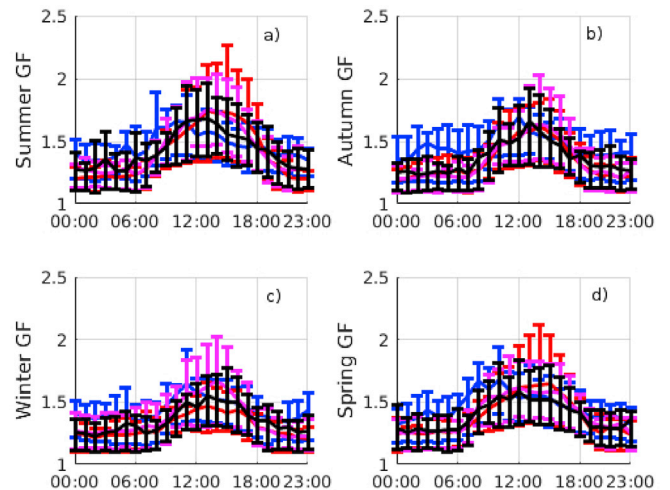
**Fig. 2.** Diurnal variation in the vertical temperature gradient (°C/m) at the Aparicio Saravia (AS; red), Jose Ignacio (JI; blue), Rosendo Mendoza (RM; black) and Colonia Eulacio (CE; magenta) towers. Vertical bars show the 16th and 84th percentiles, and the horizontal green lines mark the dry adiabatic rate,  $\Gamma_d \approx 0.01$  °C/m. Shown are: a) Summer, b) Autumn, c) Winter, and d) Spring. (For interpretation of the references to color in this figure legend, the reader is referred to the Web version of this article.)

diurnal cycle at these towers (Fig. 3) reveals that the  $GF$  was higher when the near-surface layer was less stable, i.e., during the afternoon hours.  $GF$  also varied more in the seasons with greater potentially available solar radiation, which is reasonable because larger instabilities should enhance the TKE (Stull, 1988). The gust factors at AS and CE were larger, peaked later in the afternoon, and exhibited more variability, all of which are also consistent with these sites being well-protected from the moderating influence of the ocean. In contrast, the sea-breeze strongly modulated the  $GF$  at JI, resulting in it peaking before local noon and suppressing its variability at all hours in all seasons.

Motivated by the preceding, we empirically defined the following four stability classes based on the vertical temperature gradients measured at each tower<sup>1</sup>:

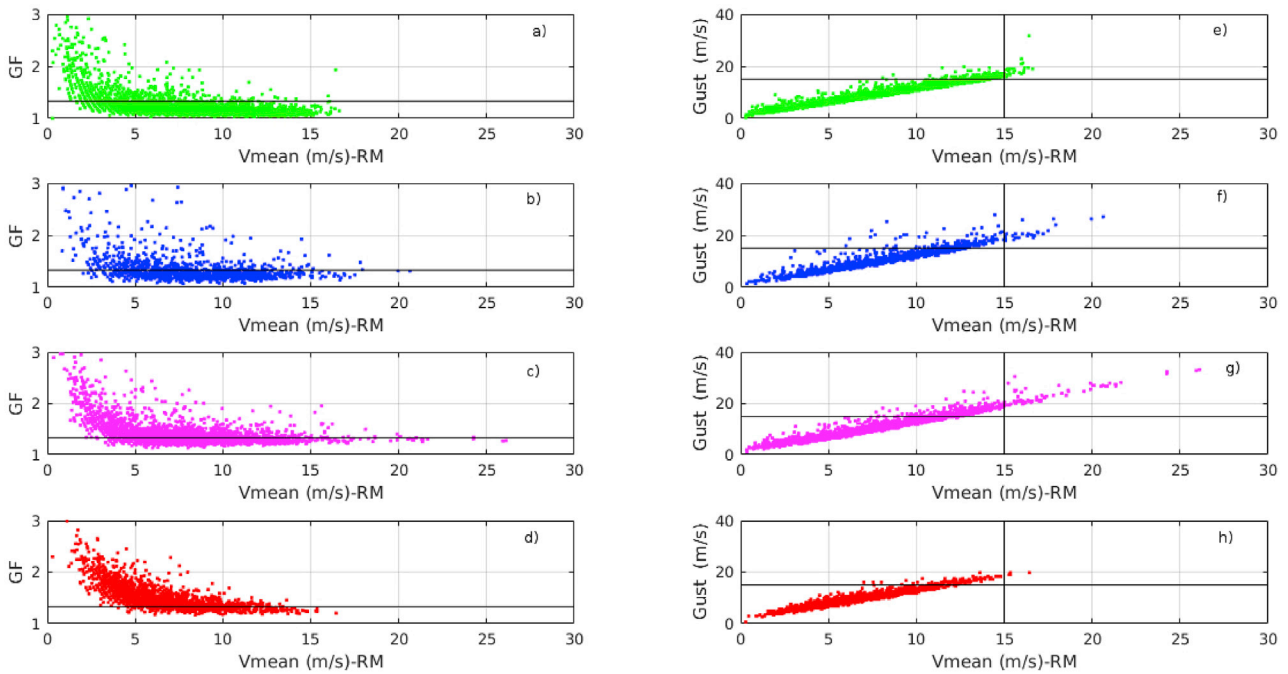
- *Strongly stable* when  $\frac{\partial T}{\partial z} \geq 0.01$  °C/m; green in the scatterplots;
- *Slightly stable* when  $0$  °C/m  $< \frac{\partial T}{\partial z} < 0.01$  °C/m; blue in the scatterplots;
- *Near neutral* (approximately dry adiabatic) when  $-0.01$  °C/m  $\leq \frac{\partial T}{\partial z} \leq 0$  °C/m; magenta in the scatterplots;
- *Absolutely unstable* (superadiabatic) when  $\frac{\partial T}{\partial z} < -0.01$  °C/m; red in the scatterplots.

Fig. 4 presents scatterplots of wind information (mean wind, gust, and  $GF$ ) representative of these stability regimes at the RM tower, which has been selected as an example. While there was a large range of gust factors at low wind speeds (when gusts are also rather weak), the  $GF$  asymptotically approached a value of about 1.33 (indicated by the black line) as



**Fig. 3.** Diurnal variation in the gust factor at tower top (about 100 m AGL) for the Aparicio Saravia (AS; red), Jose Ignacio (JI; blue), Rosendo Mendoza (RM; black) and Colonia Eulacio (CE; magenta) towers. Vertical bars show the 16th and 84th percentiles. Shown are: a) Summer, b) Autumn, c) Winter, and d) Spring. (For interpretation of the references to color in this figure legend, the reader is referred to the Web version of this article.)

<sup>1</sup> Although water vapor information is unavailable, lapse rates would only be affected if the vertical moisture gradient over the lowest 100 m was sizable.



**Fig. 4.** Gust factor vs. mean velocity (at left) and gust vs. mean velocity (at right) for the four stability regimes (top to bottom: strongly stable a), e)- green; slightly stable b), f) - blue; near neutral c), g)- magenta; and absolutely unstable d), h) - red) from the Rosendo Mendoza (RM) wind data at 101 m AGL. At left, the black horizontal lines represent an asymptotic  $GF$  value of 1.33. At right, the black horizontal lines represent gust 15 m/s, vertical black line mean velocity 15 m/s. (For interpretation of the references to color in this figure legend, the reader is referred to the Web version of this article.)

mean winds became larger (left column), independent of the stability. The decrease of  $GF$  with the mean wind is a common finding (e.g., Monahan and Armendariz, 1971; Fovell and Cao, 2017), and  $GF$  should vary with other factors, including surface roughness (Ashcroft, 1994). Gusts and mean winds were also linearly related, with relatively little scatter or slope variation among the four regimes (right column). [The lack of scatter in similar plots was noted by (Fovell and Cao, 2014; Cao and Fovell, 2018)]. Naturally, gusts were observed for all stability

conditions, but *large* gusts, which we will define as  $g \geq 15$  m/s, were relatively rare *except* when the near-surface atmosphere was nearly neutral, as also noted by (Pasquill, 1961). We will expand upon this important point soon.

These findings are also generally applicable to towers AS, JI, and CE, as shown in Fig. 5. The lack of intense gusts for strongly stable conditions (green) is not surprising, as the atmospheric stratification is preventing turbulence. Large gusts were somewhat more frequent under slightly

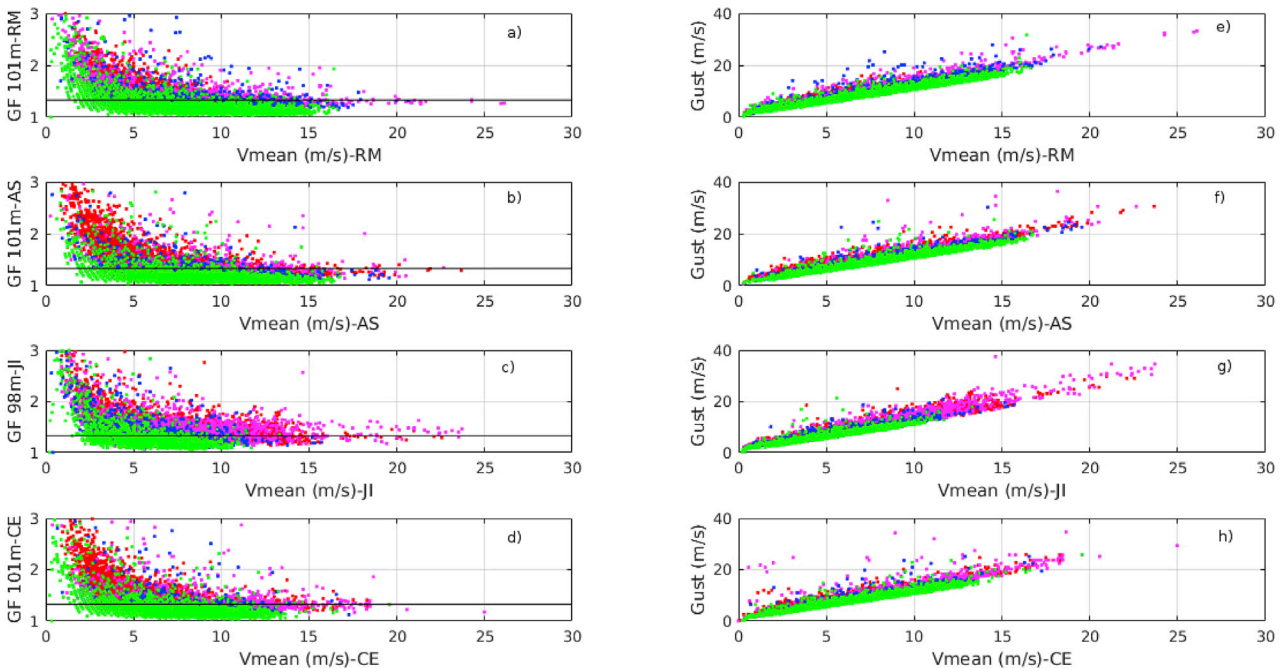


**Fig. 5.** As in Fig. 4 but superimposing all four stability regimes, for (top to bottom) RM a), e) (at 101 m AGL), AS b), f) (101 m), and JI c), g) (98 m), CE d), h) (101.8 m) towers. At left, the black horizontal lines represent an asymptotic  $GF$  value of 1.33.

stable conditions (blue); some of these could have been related to transitional conditions (from stable to unstable, or from unstable to stable). Again, gusts were most frequent under near neutral conditions (magenta). The surprising result may be the lack of sizable gusts when the vertical stratification was superadiabatic (red). This could be a consequence of strong mixing over a very deep layer, resulting in substantial momentum reduction owing to frictional influences. In any event, we need to exploit this finding in our parameterization, in order to limit the incidence of false gust alarms.

### 3.2. Large and extreme wind gust cases

Fig. 6 presents histograms of the vertical gradients of the mean wind and temperature at the Colonia Eulacio (CE) tower, again constructed from twelve consecutive months of data. The wind shear was computed using the anemometers mounted at 101.8 and 10.1 m and the temperature gradient utilized measurements taken at 100.8 and 3.4 m (Table 1). From these data, we extracted observations in which the gust  $g$  exceeded 15 and 20 m/s. The former has already been termed “large gust” and the latter threshold will henceforth be referred to as “extreme gust”. These terms are appropriate for our study area and turbine performance considerations.

From the entire dataset, it is seen that the most frequent shear value was close to zero, and a wide variety of vertical temperature gradients, both positive and negative, could occur. Significant gust observations, however, were clearly associated with larger vertical shears. At the very least, larger shear implies the existence of higher momentum parcels farther aloft that could be transported downward via turbulent motions. Note the variation of stability was small, especially for extreme gusts, and centered tightly around the dry adiabatic rate (vertical red line), which confirms our previous observation above that sizable gusts were less likely to occur when conditions were stable or superadiabatic. Note in particular that large gusts were quite uncommon when the vertical temperature profile was strongly stable ( $\frac{\partial T}{\partial z} \geq 0$ ); this fact will be exploited in our gust parameterization. Wind shears associated with extreme gusts were even larger and their association with dry adiabatic

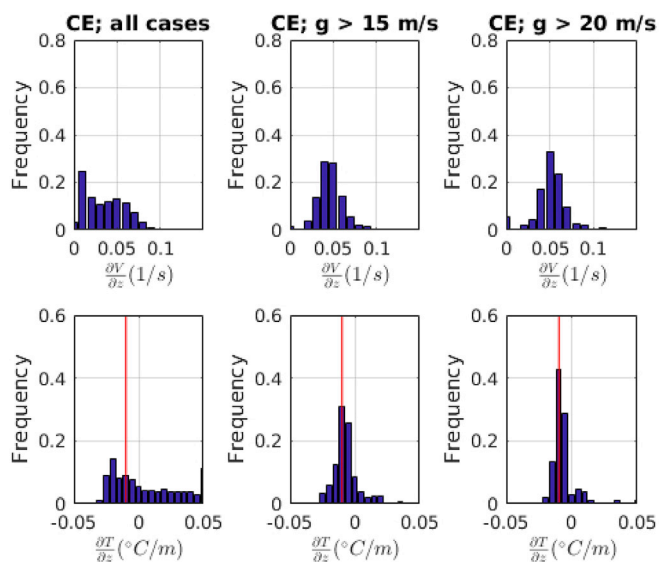


Fig. 6. Histograms of vertical wind shear (top row; 1/s) and vertical temperature gradient (bottom row; °C/m) constructed from Colonia Eulacio (CE) tower data over 12 consecutive months (spanning 2014–15). Wind data were recorded at 101.8 and 10.1 m, and temperature information at 100.8 and 3.4 m; see Table 1. The vertical red line indicates the dry adiabatic rate. Subsets representing observations with gusts  $g$  exceeding 15 and 20 m/s are also shown. (For interpretation of the references to color in this figure legend, the reader is referred to the Web version of this article.)

conditions was even more pronounced at the Atlantic Ocean site, JI (Fig. 7).

Next, we combine the observed stability and shear information via the gradient Richardson number ( $Ri$ ) estimated from the observations (Fig. 8), using the relation

$$Ri = \frac{g_0}{\Theta} \frac{\partial\Theta/\partial z}{(\partial\bar{V}/\partial z)^2}, \quad (2)$$

where  $g_0$  is the acceleration of gravity (9.8 m/s<sup>2</sup>). Potential temperature  $\Theta$  and its vertical gradient were derived from station measurements; there was insufficient moisture information to compute virtual potential temperature. At both stations, gusts exceeding even 10 m/s were very rare occurrences in the year-long records at both towers, except when  $Ri$  was within a very narrow range around zero (neutral conditions). The most frequently occurring value of  $Ri$  when large gusts appeared was  $\sim 0$ , as illustrated in the histograms of Fig. 9; this finding will be used in the gust parameterization presented below.

### 4. Numerical model and methods

Our WRF simulations used version 3.9 and employed telescoping grids with horizontal resolutions ranging from 12 to 0.444 km, the outermost domain covering a significant portion of South America (Fig. 10). The purpose of these simulations is to obtain surface and boundary layer information that can be employed in the development of a gust parameterization, and the experimental design adopted represents an attempt to maximize simulation fidelity given finite resources. Topography and landuse information were derived from the MODIS 15 s database. The 4 km nest encompassed all four tower locations, and the 1.33 and 0.444 km nests – employed for a subset of runs – surrounded the CE and RM towers. All simulations utilized 41 vertical layers with a model top of 50 hPa and the lowest model level placed at 10 m AGL. Common model physics selections include the RRTM longwave (Mlawer et al., 1997) and Dudhia shortwave (Lacis and Hansen, 1974; Stephens, 1978) radiation schemes, Lin microphysics (Lin et al., 1983), and the Noah land surface model (Chen and Dudhia, 2001). The Kain–Fritsch (Kain, 2004; Kain and Fritsch, 1990) cumulus parameterization was employed in the 12 km domain only.

Sensitivity to the planetary boundary layer treatment was assessed via a physics ensemble consisting of eight PBL schemes: YSU (Hong et al.,

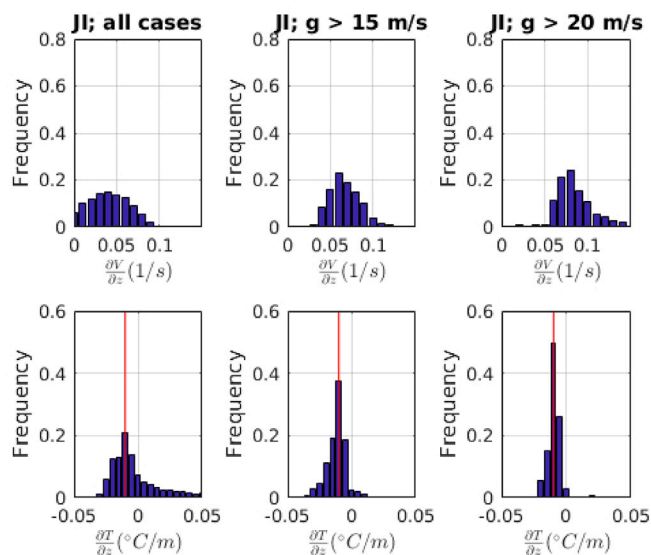


Fig. 7. Similar to Fig. 6 but for the Jose Ignacio (JI) tower. Both wind and temperature data were recorded at 98 and 12 m over a calendar year (2012); see Table 1.

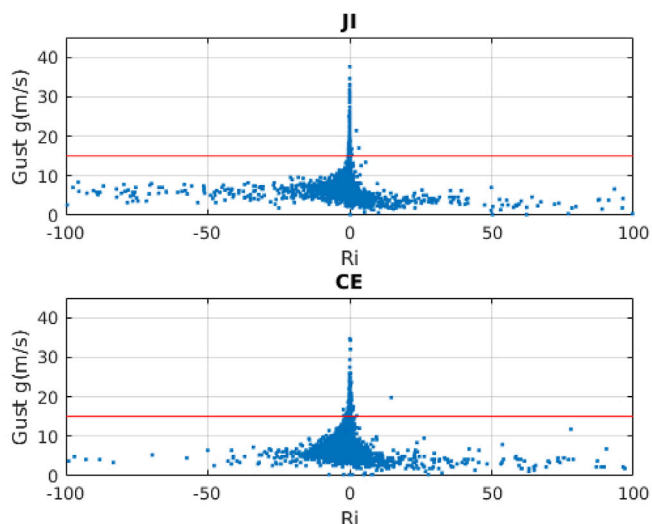


Fig. 8. Scatterplot of Richardson number  $Ri$  and gust  $g$  (m/s) for the Jose Ignacio tower (JI, top), and for the Colonia Eulacio tower (CE, bottom), both computed from twelve consecutive months of observations.

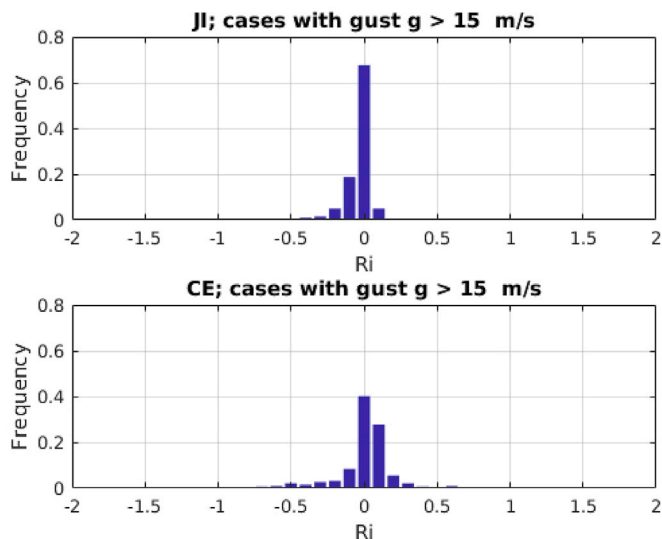


Fig. 9. Data from Fig. 8, expressed as a histogram, but only for observations with large gusts ( $g > 15$  m/s).

2006), MYJ (Mellor and Yamada, 1974, 1982), ACM2 (Pleim, 2007a, 2007b), BouLac (Bougeault and Lacarrere, 1989), Bretherton–Park (Bretherton and Park, 2009), GBM-TKE (Grenier and Bretherton, 2001), Shin–Hong (Shin and Hong, 2015), and MYNN 2.5 (Nakanishi, 2001). For each, the most commonly adopted surface layer scheme was used. For runs utilizing the two innermost (1.33 and 0.444 km) nests, we elected to focus on the Shin–Hong and MYJ schemes. The recently introduced Shin–Hong scheme is “scale-aware”, reducing the parameterized mixing as the grid spacing is refined, and MYJ was developed for operational models at the National Centers for Environmental Prediction (NCEP).

The simulations analyzed herein utilized the NCEP Global Forecast System operational global analyses for the initial and boundary conditions, and the model was run from the period 8 August 2014 to 7 August 2015, inclusive, with a focus on comparing simulations with measurements available from wind cup anemometers at  $\sim 100$  m AGL. During this period, only data from the RM and CE towers were available for prediction and verification, so our analyses are limited to that geographic region. The year-long period was divided into thirteen, non-overlapping

simulation segments, each commencing with a cold start generally on the first of the month. Analysis nudging was employed (in the outermost domain only) to prevent significant simulation drift but sea-surface temperature was not updated during each segment. Although Skamarock, 2004 demonstrates that WRF model spectra can “spin-up” in 6 h or less, and spin-up periods of 12 h or less have been employed in recent studies of mesoscale phenomena (e.g., Smith et al., 2017; Li and Chen, 2017; Brown and Reuter, 2018; Fernández-González et al., 2018), we have neglected the first full 24 h period of each simulation segment in our analyses. This had only a very small effect on the results.

We will compare the gust parameterization we develop to the algorithm for non-convective gusts<sup>2</sup> employed at the European Center for Medium-Range Weather Forecasting (ECMWF), based on (Panofsky et al., 1977):

$$g_{EC} = \bar{V} + 7.71u_* \tag{3}$$

in which the gust  $g_{EC}$  is a function of mean horizontal velocity  $\bar{V}$  and friction velocity  $u_*$ . Although apparently developed for 10 m AGL, we will assess its applicability to forecasting gusts at the turbine hub height of  $\sim 100$  m.

## 5. Numerical simulations and gust parameterization development

### 5.1. PBL results and sensitivity in the 4 km experiments

Tower observations have demonstrated that neutral surface layer conditions were conducive to the appearance of large gusts at hub height, suggesting that the Richardson number could be a useful component of a gust parameterization. However, successful application of this finding to numerical model output requires that the surface layer be simulated with reasonable fidelity. This involves accurate predictions from the PBL, surface layer, and land surface parameterizations. In this section, we examine the performance of WRF simulations using eight different PBL treatments (along with their typical surface layer schemes) utilizing the 12- and 4-km domains. All simulations employed the Noah land surface model.

Figs. 11 and 12 present histograms of vertical shears and temperature gradients, respectively, computed using forecasts on model levels (e.g., 10 and 100 m AGL) nominally within the surface layer and roughly corresponding to measurement heights at the CE tower (selected as an example), but only when observed gusts exceeded 15 m/s. Recall from Fig. 6 that large gust observations coincided most frequently with shears between 0.04 and 0.05 1/s. It is obvious that the vertical shear was underpredicted by all eight PBL ensemble members, especially the BouLac scheme. As these PBLs represent a variety of surface layer treatments, but a common land surface model, some of the problem may reside in the latter, perhaps involving insufficient surface roughness.

Temperature gradients associated with large gust conditions were also generally underspecified. In the observations (Fig. 6, bottom middle plot), the dry adiabatic lapse rate appeared most frequently, but steeper gradients also occurred, and substantial gustiness was quite rare under strongly stable conditions. In contrast, most of the PBL ensemble members were predicting somewhat more stable lapse rates, and substantially superadiabatic lapse rates were rarely produced (Fig. 12). This result may have been different had diagnosed 2 m temperatures (generated by the surface layer scheme) been used, especially as that level is closer to the lower observation height of temperature of 3.4 m for this tower (Table 1). However, we elected to construct our parameterization using directly predicted quantities, for practical reasons: we are using the same model

<sup>2</sup> The ECMWF approach includes an augmentation term when convective activity is expected.

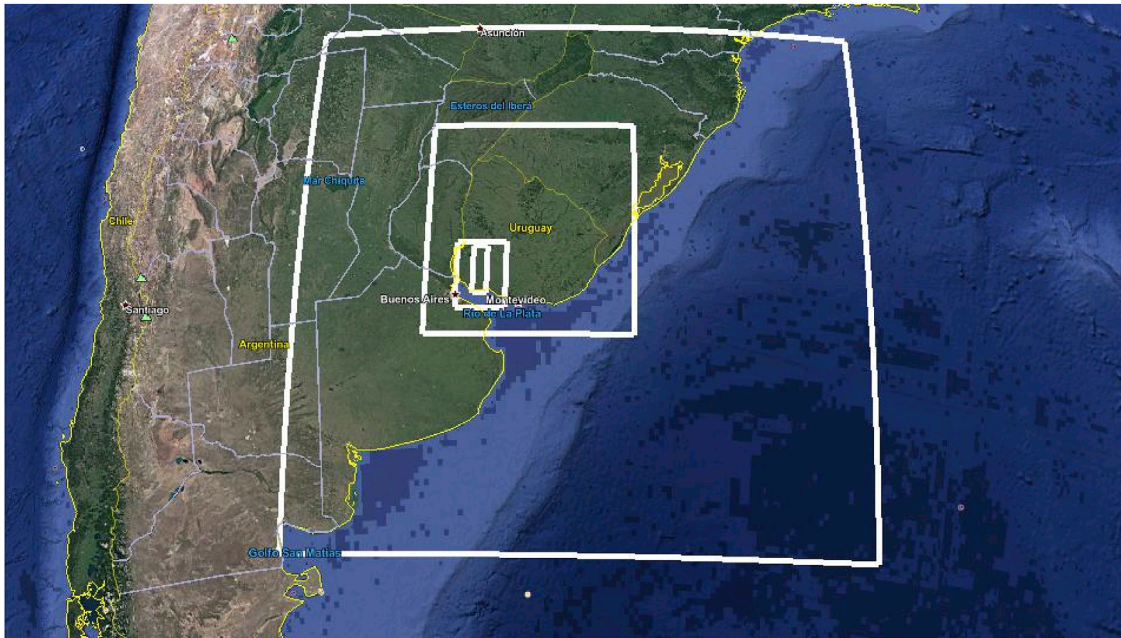


Fig. 10. Telescoping Weather Research and Forecasting (WRF) domains with horizontal grids of 12, 4, 1.33, and 0.444 km.

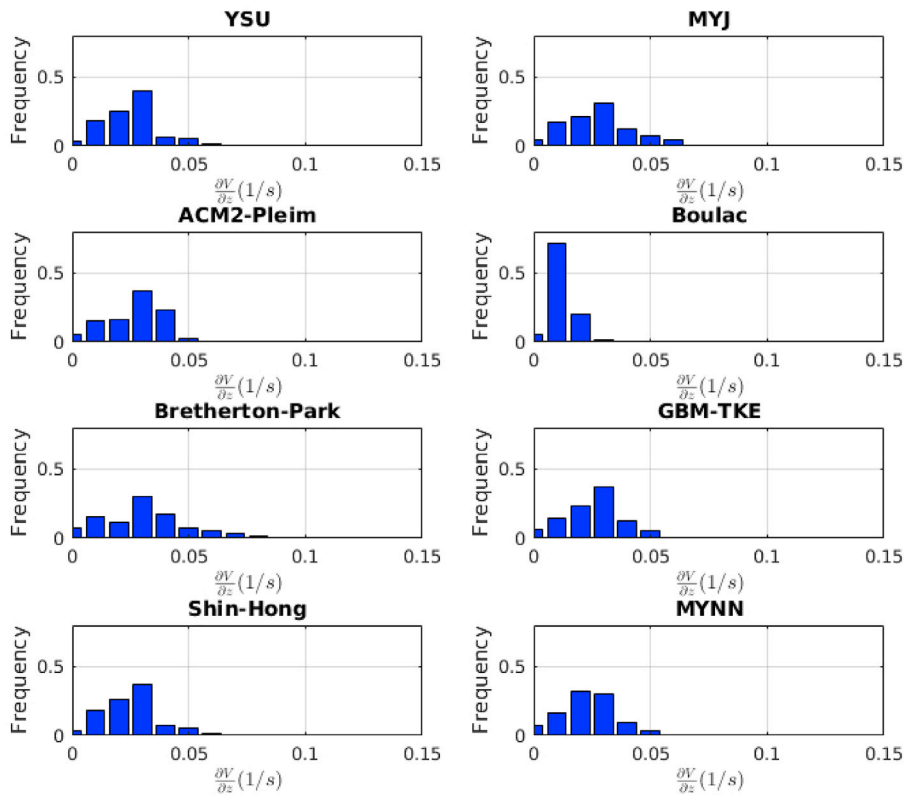


Fig. 11. Histograms of vertical wind shear  $\frac{\partial V}{\partial z}$  (1/s) between 100 and 10 m AGL in cases where  $g > 15$  m/s at the top of the CE tower (101.8 m AGL), simulated with PBL schemes YSU, MYJ, ACM2, BouLac, Bretherton–Park, GBM–TKE, Shin–Hong, and MYNN, with a horizontal grid resolution of 4 km.

levels for both vertical gradients as well as values subject to fewer assumptions.

Recall from Fig. 9 that observed  $Ri$  values tightly clustered around zero (neutral conditions) during large gust conditions at the CE tower, with positive values being somewhat more common than negative ones at that location. As simulated temperature gradients were a little too

stable and shears were generally underestimated, at least for  $g > 15$  m/s observations, model simulated Richardson numbers can be expected to have a high bias. Despite that, Fig. 13 indicates that, apart from the BouLac result, the simulated distributions of  $Ri$  computed from the WRF simulations were not unacceptable, with  $Ri \approx 0.1$  being the most common result for most of the schemes. The principal issue is that the range

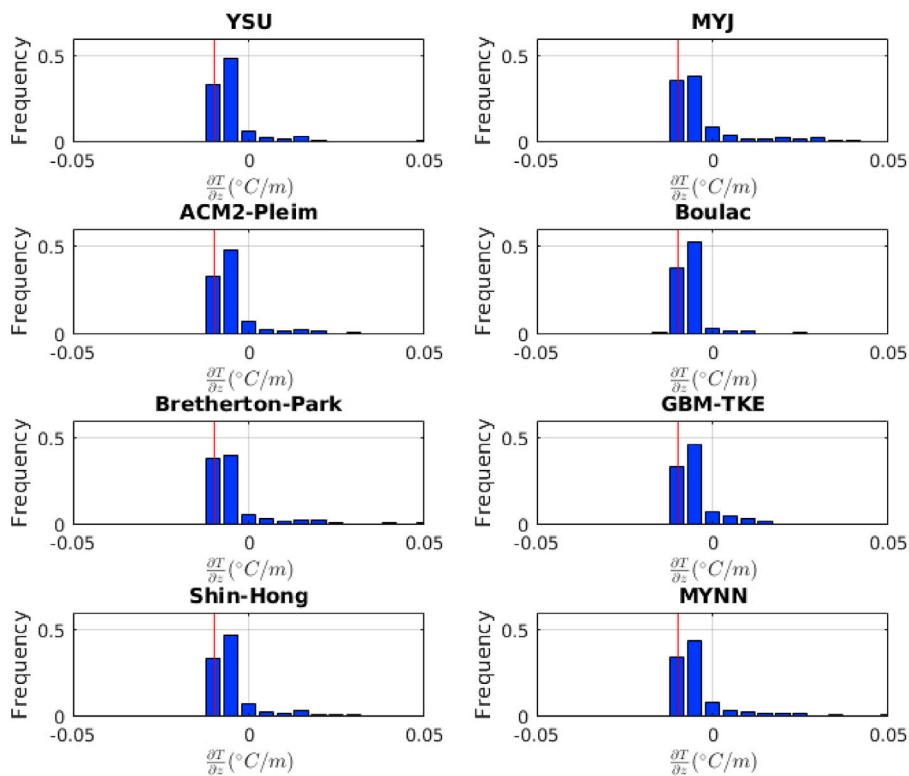


Fig. 12. As in Fig. 11, but for the vertical temperature gradient  $\frac{\partial T}{\partial z}$  ( $^{\circ}\text{C}/\text{m}$ ) at CE tower. Vertical red lines mark the dry adiabatic lapse rate. (For interpretation of the references to color in this figure legend, the reader is referred to the Web version of this article.)

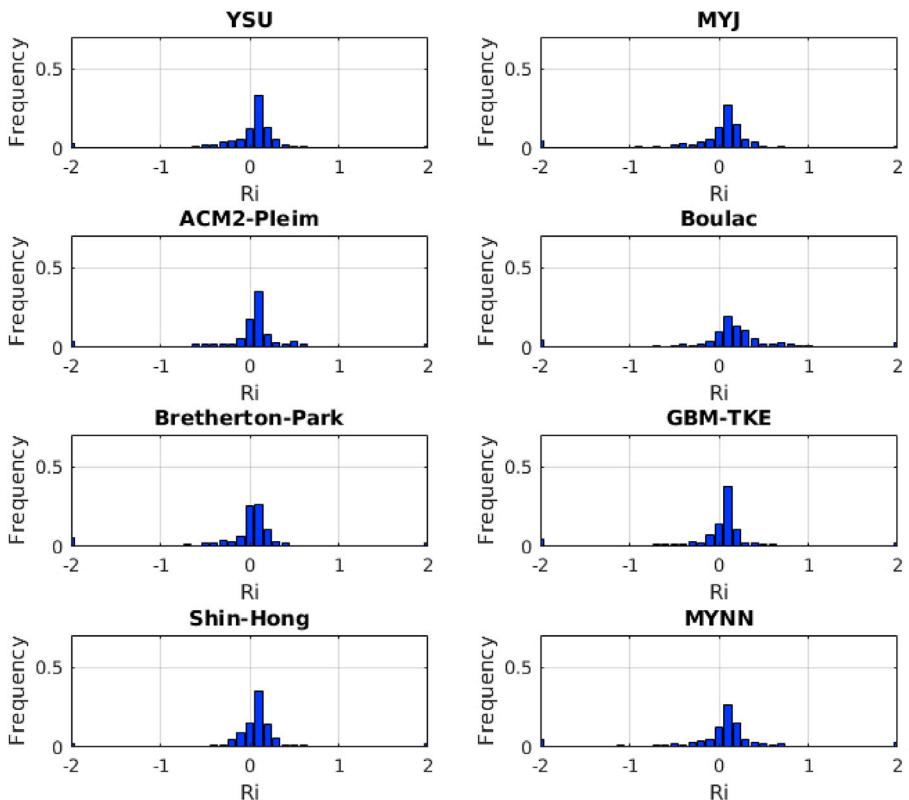
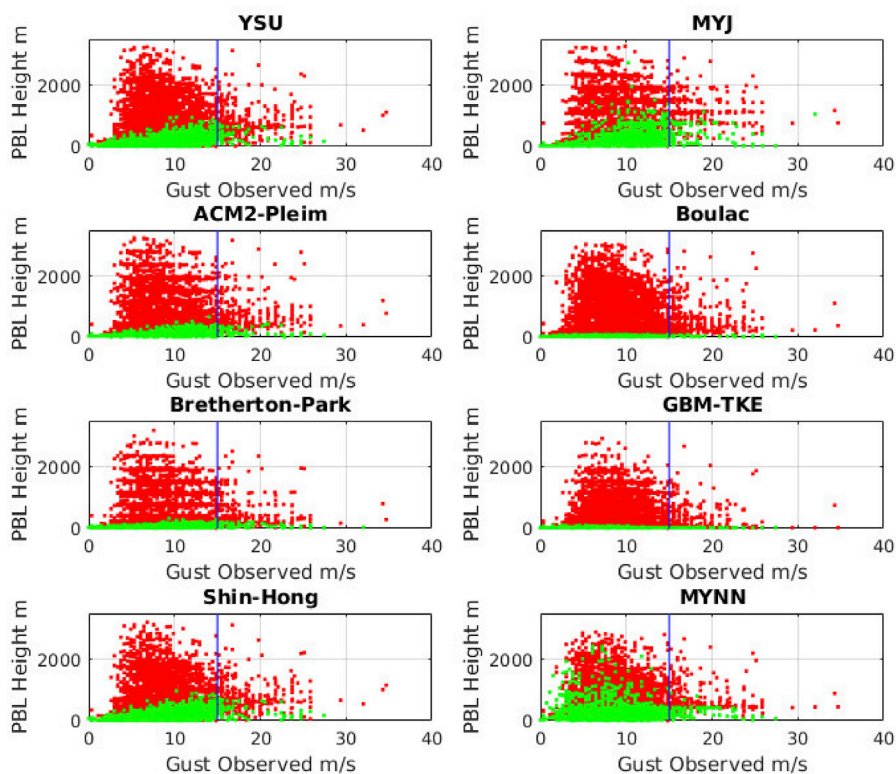


Fig. 13.  $Ri$  computed from 4-km WRF simulations using the eight planetary boundary layer schemes at CE tower when the observed gust was  $> 15$  m/s.



**Fig. 14.** Predicted PBL heights vs. observed gusts for the CE tower location, from 4-km WRF simulations using the eight PBL schemes. Green dots indicate strongly stable conditions ( $\frac{\partial T}{\partial z} > 0$ ), computed from the simulations. Large gust (15 m/s) threshold indicated. (For interpretation of the references to color in this figure legend, the reader is referred to the Web version of this article.)

of simulated  $Ri$  values associated with large gust conditions was too large in all cases. Thus, the gust parameterization will have to tolerate some imprecision and bias in the  $Ri$  calculation.

PBL schemes also estimate boundary layer depth, and we have attempted to see if this information would be useful to the gust parameterization. Figs. 14 and 15 present scatterplots of observed gust vs. simulated PBL height for the CE tower, color coded by the vertical temperature gradient derived from the simulations and the observations, respectively, for all eight PBL schemes. A green marker indicates strongly stable  $\frac{\partial T}{\partial z} \geq 0$  conditions, while red markers are used for all other observations. In all plots, the vertical blue line marks the large gust limit of 15 m/s.

Section 2 revealed that extreme gust occurrence had a significant stability dependence. We again see that large gusts were again quite rare when the resolved surface layer was strongly stable (green dots in Fig. 15) and this tendency was faithfully reproduced in the WRF runs (Fig. 14), at least in bulk and for most of the parameterizations. It is also clear that sizable gusts were not associated with large PBL depths. In those cases, it appears that vertical mixing over a substantially deep layer reduced the chances of large winds appearing at hub height. Instead, the substantial majority of large gusts occurred when the stratification was less stable but the boundary layer was not deep. Unfortunately, shallower PBLs also frequently occurred when the gusts were not strong. This motivated us to factor stability but not PBL depth into our gust parameterization.<sup>3</sup>

<sup>3</sup> Large gusts could be made conditional on shallow PBL depths in a future version of this parameterization.

## 5.2. Proposed gust parameterization

We now propose a refined version of the gust parameterization (GP) presented in (Gutiérrez and Fovell, 2015). The approach involves not predicting the gust directly but rather anticipating the appropriate gust factor  $GF$ , which is then applied to a simulated wind to yield a forecast for gusts. The refinement not only simplifies the algorithm but also makes it more directly aware of the ambient stability and vertical shear that could help capture sizable gusts that occur in marginal stability conditions. To permit a more detailed presentation of the wind gust formulation, the focus of the analysis will be on one twelve-month period, during which only CE and RM tower data were available.

As we have shown, the largest gusts require near-neutral surface layers ( $Ri \sim 0$ ), copious vertical shear, and shallow (as opposed to deep) PBLs. If  $Ri$  is too negative, it is probably because there is insufficient vertical shear to support gustiness. If the PBL is too deep, the momentum is probably mixed too thoroughly for gusts to emerge at hub height. If the vertical stability is too large, mixing is likely very suppressed, even under highly sheared conditions. We have also shown that  $GF$  tends to vary inversely with the magnitude of the sustained wind but also be larger during less stable conditions (e.g., Figs. 3 and 4). These characteristics are incorporated, directly or indirectly, into our GP.

The new parameterization consists of a first-guess  $GF$  that is subsequently modified under particularly favorable conditions. The first-guess  $GF$  is given by a minimum value ( $GF_{min}$ ) that is augmented by a stability-dependent function of the model predicted winds at and above the hub ( $\approx 100$  m) height, given by:

$$GF = GF_{min} + K \frac{\Delta V^{Top}}{V_{100}}, \quad (4)$$

where  $K$  is a slope,  $V_{100}$  is the wind speed forecasted at hub height, and

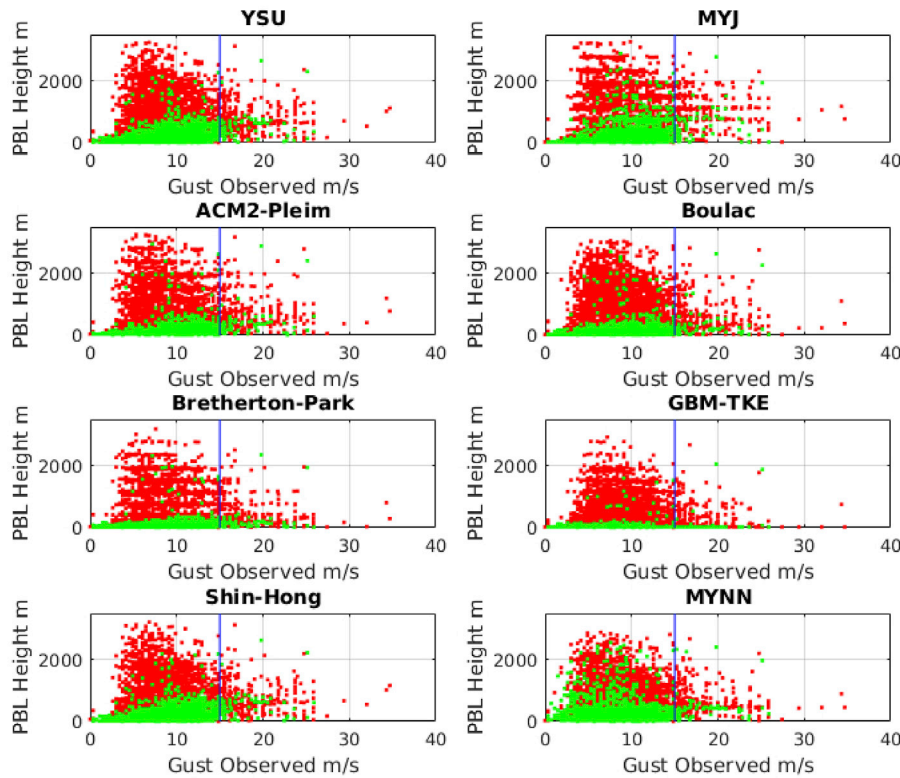


Fig. 15. As in Fig. 14, but using vertical stabilities computed using observations taken at CE tower.

$\Delta V^{Top} = \max(0, V_{MAX} - V_{100})$  is a vertical speed difference.  $V_{MAX}$  is generally taken to be the wind speed at the PBL top, except under strongly stable ( $\frac{dT}{dz} \geq 0$ ) conditions, in which the wind at 200 m (twice the hub height) is used. This empirical selection reflects the expectation that vertical mixing is strongly suppressed under isothermal and positive temperature gradients, and helps to reduce false gust alarms.

The parameters  $GF_{min}$  and  $K$  were determined via least squares, but also made a function of wind speed by binning the data into discrete categories with respect to simulated  $V_{100}$ . Different coefficients were also estimated for strong stability conditions and values were determined separately for each PBL scheme and model resolution, in order to refine forecasts and help mitigate biases. As an example, Fig. 16 presents the best-fit coefficients computed using the Shin–Hong PBL scheme at horizontal grid resolutions of 12 km and 0.444 km using CE tower information. As anticipated from the observations (e.g., Figs. 3 and 4),  $GF_{min}$  varies inversely with the hub height wind speed but is generally larger for less stable stratification and smaller for finer scale simulations. The  $K$  coefficient was also found to have some wind speed, stability, and resolution sensitivity. The best fits obtained for the other schemes were qualitatively quite similar (not shown).

The tentative gust forecast is the product of the first-guess  $GF$  and the simulated hub-height wind  $V_{100}$ . We found this skillfully discriminated between small and large gusts, which is important for wind turbine operations, but tended to underestimate the magnitudes of the latter, which are also of considerable interest. This was remedied by making this further modification to the parameterization, but only when the tentative gust exceeded 11.5 m/s and the forecast  $Ri$  was near zero (specifically,  $-0.1 < Ri < 0.3$ ):

$$GF = S_{Ri} \left( GF_{min} + K \frac{\Delta V^{Top}}{V_{100}} \right), \tag{5}$$

in which  $S_{Ri}$  was empirically determined to be 1.15. The asymmetric  $Ri$  range was motivated by Fig. 13 and reflects model limitations. This modification helped the model capture gusts occurring during conditions

most likely associated with large wind bursts: the presence of significant shear, and Richardson numbers in the vicinity of 0. This approach has proved skillful for other towers as well (not shown), but only for the PBL schemes that resulted in reasonably accurate predictions of  $Ri$ .

### 6. Gust forecasting skill

In this section, the skill of the new GP is assessed and compared to the

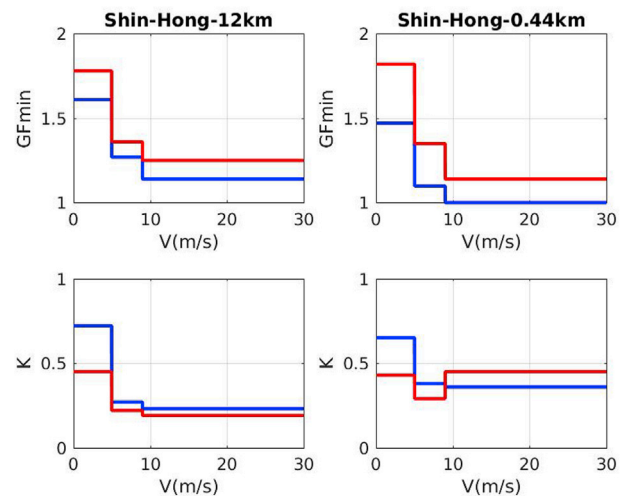


Fig. 16.  $K$  and  $GF_{min}$  fit optimally with information from CE tower observations and simulations using the Shin–Hong scheme with horizontal grid resolutions of 12 km and 0.444 km. Blue represents  $\frac{dT}{dz} \geq 0$  and red represents  $\frac{dT}{dz} < 0$ , computed from the simulations. Velocity intervals applied to WRF forecasts were  $0 \text{ m/s} < V \leq 5 \text{ m/s}$ ,  $5 \text{ m/s} \leq V < 9 \text{ m/s}$  and  $9 \text{ m/s} \leq V$ . (For interpretation of the references to color in this figure legend, the reader is referred to the Web version of this article.)

ECMWF model (3) at the RM tower, which is located in relatively flat terrain near an estuary of the La Plata river. The 8 PBL configurations employed in the 12 and 4 km simulations are augmented with Shin–Hong and MYJ runs using higher resolution nests of 1.33 and 0.444 km. By its nature, the ECMWF formula is essentially location-independent, although local surface roughness appears indirectly owing to the friction velocity. Here, we use the GP to forecast RM tower gusts utilizing  $GF_{min}$  and  $K$  values derived for each PBL scheme and resolution at the CE tower, both residing within the 1.33 (and 0.444) km domains. It is recognized that tuning the GP specifically to the RM tower information would result in higher skill, but this test helps illustrate how applicable the gust model is to a different location in the same geographic region.<sup>4</sup> The emphasis is on producing a skillful alarm for large gust events.

### 6.1. First-guess gusts and forecast biases

The top row of Fig. 17 displays forecast  $Ri$  vs. first-guess GP-diagnosed gusts, color-coded by the observed gust magnitude (magenta for  $g > 15$  m/s, blue otherwise), for the RM tower from 4-km simulations using the Shin–Hong PBL. As at CE and JI tower (Fig. 9), the substantial majority of large gusts ( $g > 15$  m/s) occurred when the measured  $Ri$  was close to 0. The concentration of magenta dots near forecast  $Ri \sim 0$  reveals that the simulations were successful in recreating the conditions that existed when large gusts were observed. Note that large gusts were quite rare when  $Ri \neq 0$  was predicted.

However, as illustrated by the histogram of gust error (forecast–observed) in the bottom left panel, gust strength was generally under-predicted when large values were observed. This error distribution motivated the adjustment (5) discussed above. The panels at right in Fig. 17 incorporate gust forecasts from (5) with  $S_{Ri} = 1.15$  when the first-guess gust  $> 11.5$  m/s and the forecast  $Ri$  was near zero. This adjustment more accurately captures the largest gusts, and centers the error distribution about zero (Fig. 17, bottom right). It also obviously helps concentrate the magenta points even more narrowly around model-estimated  $Ri = 0$ , representing a further improvement in skill (Fig. 17, top right). It is important to note that the  $S_{Ri}$  value of 1.15 was selected based on minimizing the bias at CE tower (not shown). It is clear, however, that it accomplished the same goal when applied to RM forecasts.

### 6.2. Wind gust alarms

In (Friederichs et al., 2009), it was argued that reliable forecasts of wind gusts offer the potential to mitigate the destruction and human loss they cause, and to better plan for disruptions and subsequent clean-up operations. Key users of gust warnings are emergency managers, air and rail traffic controllers, energy companies, and the general public. This is particularly critical for energy systems with high levels of wind power participation, such as the Uruguayan system (UTE, 2017). Thus, improving the quality of gust warnings is of great importance, particularly motivating methods that can be adapted to different gust thresholds.

In the present work, a true alarm (TA) was assigned when both the observation and the wind gust forecast exceeded our selected large gust threshold of 15 m/s, and the true alarm rate (TAR) is the ratio of correct forecasts and observed large gusts. (TAR is also referred to as the Probability of Detection, or POD.) A false alarm (FA) is assigned instead if the gust forecast was larger than the threshold but the observed value was not, and the false detection rate (FDR) is the fraction of all large gust forecasts that were in error. FDR is preferred in this application as the number of non-large gust observations and predictions is very large, which makes the false alarm rate (FAR) deceptively small.<sup>5</sup> A missed

event (ME) occurs when the forecast failed to detect an observed large gust.

Since it is unrealistic to assume that a model can skillfully predict a large gust at its precise time of occurrence, a range of time windows, centered on the forecast time, are also considered. For example, with a 1-h window, a predicted gust exceeding 15 m/s would count as a TA if a large gust occurred within 30 min of the forecast time. As gusty events could result in abrupt changes to power production that need to be anticipated in the operation of an electrical system, especially owing to staffing considerations, 6- and 12-h periods also represent useful window lengths.

### 6.3. Skill of forecast gust with respect to horizontal grid resolution

We now directly compare the GP gust forecasts with those using the ECMWF method as a function of model grid resolution and time interval, again for the RM tower and focusing first on simulations made using the Shin–Hong PBL scheme. In Fig. 18's scatterplots, a red point indicates an observed gust exceeded 15 m/s within either 1 or 12 h windows. During the year-long simulation period (whitout first day each WRF running), there were 8448 hourly gust observations, of which 831 (~10%) exceeded 15 m/s. Among the year's 704 non-overlapping 12-h windows, there were 205 (29%) instances of one or more large gusts.

The purpose of this effort is to determine the grid spacing necessary to attain the desired skill for both gust models under consideration. Separate analyses were performed for simulations with highest resolutions of 12, 4, 1.33, and 0.444 km, with the four quadrants of each plot representing: (a) TA-GP and ME-ECMWF; (b) TA-GP and TA-ECMWF; (c) ME-GP and ME-ECMWF; and (d) ME-GP and TA-ECMWF. The figure reveals that there is a substantial, if somewhat resolution-dependent, correlation between the GP and ECMWF gust estimates as well as skill for both with respect to discriminating between large and small gusts. There were necessarily fewer independent events in the much wider 12-h window (panels at bottom), but the overall relationship between the two gust models is similar.

Table 2a (12 and 4 km) and Table 2b (1.33 and 0.444 km) reveals that the GP model captured 52% (= TAR) of the observed gusts in the 1-h window when the Shin–Hong scheme was used when the highest horizontal resolution was 12 km. The TAR with this scheme was as high as 61% when finer grid spacings were employed. In contrast, the ECMWF method benefits from or requires higher resolution, as it only captured 36% of true alarms in the 1-h window with the 12-km simulations, but this increased to 63% when the 0.444 km nest was used. Note in particular the appearance of red dots in the upper left quadrants, representing events captured by the GP but missed by ECMWF. Direct incorporation into the GP of stability and shear information computed on model levels is believed to account for its enhanced skill, especially when lower horizontal resolution is employed.

Red dots in quadrant (c) represent missed events. Some of these are very likely associated with convective storms, that might require additional physics term in the parametrization formulation, which have been ignored herein but will be examined in future work. Regarding false alarms, GP's FDR declined from 52 to 43% as the resolution improved, while for ECMWF the false detection rate remained close to 50% in this narrow time window. Unfortunately, this means that for both gust models, even without explicit consideration of convective gusts, a large fraction of the gust alarms proved to be incorrect.

This result motivates consideration of wider verification time windows. However, expanding this interval had a complex and resolution-dependent effect on skill with this as well as other PBL schemes. For both gust models, the TA rate reliably improved only with grid spacings finer than 12 km. FDR, in contrast, declined significantly with grid refinement, reaching 20 and 25% in the 0.444 km runs for GP and ECMWF, respectively, with the Shin–Hong parameterization. Note that some schemes, notably BouLac, had relatively small false detection rates. However, this came as a consequence of its low TARs, reflecting the

<sup>4</sup> Note the RM tower only has one anemometer, so vertical shear cannot be determined observationally anyway (see Table 1. The vertical red line indicates the dry adiabatic rate.).

<sup>5</sup> Note that TAR and FDR do not sum to 100%.

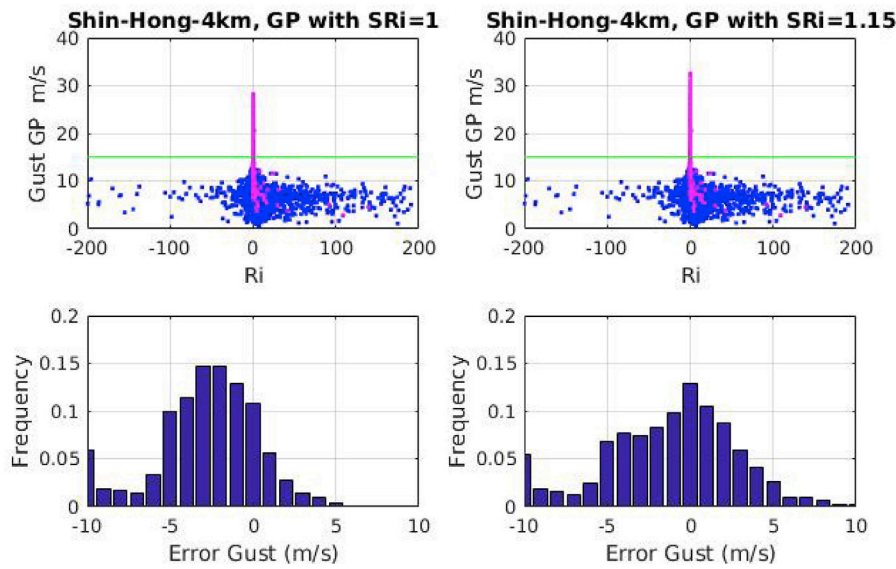


Fig. 17. Results for RM tower from simulations using the Shin-Hong PBL at 4 km resolution. Top row: GP-diagnosed gust (m/s) vs. forecast  $R_i$ , color-coded by the magnitude of the observed gust (magenta for  $g > 15$  m/s, blue otherwise). Bottom row: Histogram of errors (forecast-observed) for gust predictions when large gusts were observed. Left (right) panels show GP with  $S_{Ri} = 1.0$  (1.15). (For interpretation of the references to color in this figure legend, the reader is referred to the Web version of this article.)

scheme's difficulty in simulating observed  $R_i$  values.

Considering TAR and FDR jointly, as well as computational efficiency, we believe the most useful single forecasts were those produced by the GP employing Shin-Hong PBL at 4 km resolution, which attained a TAR of 70% against an FDR of 24%. Especially since 4 km runs are significantly less expensive to operate, it is a simple matter to combine forecasts using both gust models and different PBL parameterizations to create an ensemble mean with further enhanced skill. Although beyond the scope of this study, MYNN forecasts might be included in the ensemble owing

to its relatively high TAR, especially with ECMWF, as a particular example.

### 7. Conclusion

Gust forecasting is important, especially for electric utilities with high levels of wind power participation, such as the Uruguayan system. A gust parameterization (GP) has been developed, utilizing information from numerical weather prediction models and both motivated by and verified

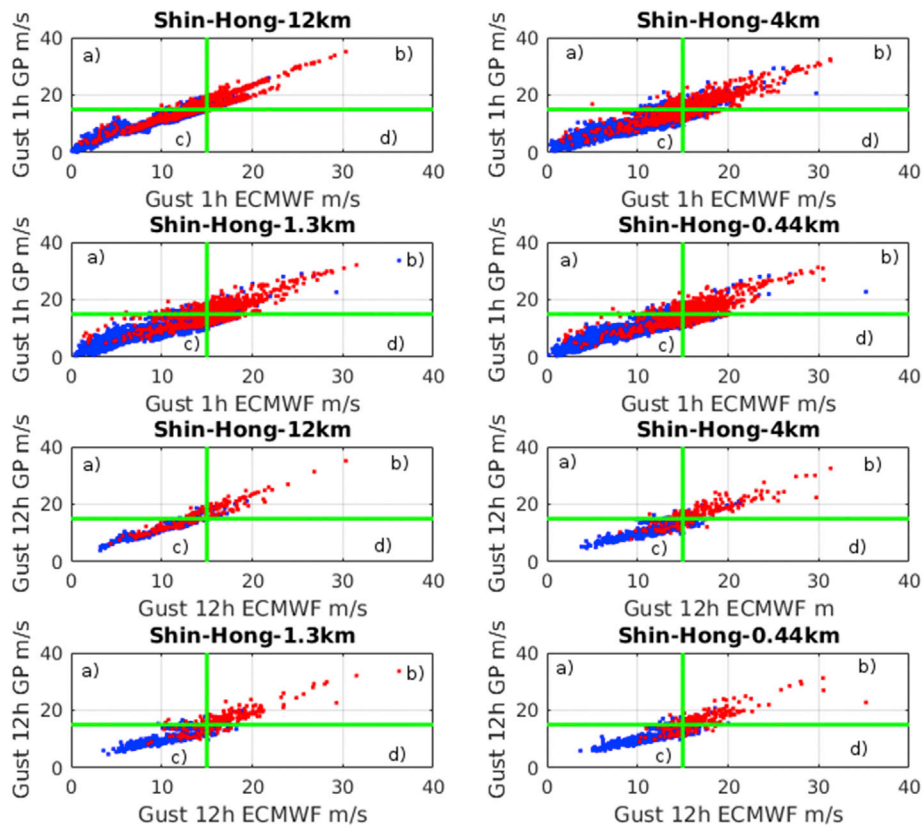


Fig. 18. ECMWF vs. GP (m/s) gust forecasts at the RM tower, using the Shin-Hong PBL scheme at 12 km, 4 km, 1.33 km, and 0.444 km horizontal grid resolution, and time windows of 1-h (top) and 12-h (bottom). Red dots show gusts exceeding  $g > 15$  m/s over the time interval being considered. (For interpretation of the references to color in this figure legend, the reader is referred to the Web version of this article.)

**Table 2a**

True alarm rate (TAR) and false detection rate (FDR) conditions for RM tower forecasts between August 8, 2014, and August 7, 2015, based on gust model (ECMWF and GP), simulation resolution (12 and 4 km) and time window length (1, 6, and 12 h), for selected PBL schemes. N = number of individual events.

		YSU	MYJ	Pleim	Boulac	B-P	GBM	S-H	MYNN
ECMWF	TAR	37%	37%	41%	39%	36%	39%	36%	38%
1h window 12km N=831	FDR	47%	44%	48%	44%	46%	44%	47%	43%
GP	TAR	51%	52%	53%	48%	54%	48%	52%	52%
1h window 12km N=831	FDR	50%	54%	49%	47%	55%	47%	52%	50%
ECMWF	TAR	36%	37%	40%	38%	36%	38%	36%	38%
6h window 12km N=275	FDR	30%	28%	31%	28%	30%	28%	30%	26%
GP	TAR	44%	48%	44%	45%	48%	45%	46%	50%
6h window 12km N=275	FDR	27%	33%	27%	27%	30%	27%	27%	34%
ECMWF	TAR	37%	38%	40%	38%	37%	38%	37%	39%
12h window 12km N=205	FDR	22%	21%	24%	22%	23%	22%	22%	21%
GP	TAR	44%	50%	44%	45%	50%	45%	46%	51%
12h window 12km N=205	FDR	21%	26%	21%	22%	24%	22%	20%	29%
ECMWF	TAR	55%	61%	61%	51%	64%	60%	55%	69%
1-h window 4km N=831	FDR	55%	59%	53%	53%	63%	55%	54%	56%
GP	TAR	60%	60%	59%	46%	61%	64%	61%	54%
1-h window 4km N=831	FDR	48%	51%	47%	47%	54%	55%	48%	45%
ECMWF	TAR	64%	69%	67%	56%	79%	68%	64%	78%
6h window 4km N=275	FDR	42%	49%	41%	41%	51%	45%	42%	46%
GP	TAR	66%	67%	64%	53%	72%	72%	69%	61%
6h window 4km N=275	FDR	33%	40%	33%	33%	45%	44%	32%	31%
ECMWF	TAR	66%	72%	68%	56%	83%	71%	64%	80%
12h window 4km N=205	FDR	32%	40%	35%	33%	41%	37%	33%	38%
GP	TAR	67%	70%	65%	54%	76%	73%	70%	62%
12h window 4km N=205	FDR	25%	33%	26%	24%	38%	38%	24%	26%

**Table 2b**

True alarm rate (TAR) and false detection rate (FDR) conditions for RM tower forecasts between August 8, 2014, and August 7, 2015, based on gust model (ECMWF and GP), simulation resolution (1.33 and 0.444 km) and time window length (1, 6, and 12 h), for selected PBL schemes. N = number of individual events.

		YSU	MYJ	Pleim	Boulac	B-P	GBM	S-H	MYNN
ECMWF	TAR	–	–	–	–	–	–	64%	56%
1h window 1.33km N=831	FDR	–	–	–	–	–	–	52%	48%
GP	TAR	–	–	–	–	–	–	56%	57%
1h window 1.33km N=831	FDR	–	–	–	–	–	–	45%	44%
ECMWF	TAR	–	–	–	–	–	–	72%	66%
6h window 1.33km N=275	FDR	–	–	–	–	–	–	41%	36%
GP	TAR	–	–	–	–	–	–	65%	65%
6h window 1.33km N=275	FDR	–	–	–	–	–	–	33%	29%
ECMWF	TAR	–	–	–	–	–	–	75%	67%
12h window 1.33km N=205	FDR	–	–	–	–	–	–	32%	30%
GP	TAR	–	–	–	–	–	–	67%	65%
12h window 1.33km N=205	FDR	–	–	–	–	–	–	25%	22%
ECMWF	TAR	–	–	–	–	–	–	69%	63%
1h window 0.44km N=831	FDR	–	–	–	–	–	–	54%	48%
GP	TAR	–	–	–	–	–	–	57%	55%
1h window 0.44km N=831	FDR	–	–	–	–	–	–	46%	43%
ECMWF	TAR	–	–	–	–	–	–	79%	72%
6h window 0.44km N=275	FDR	–	–	–	–	–	–	41%	34%
GP	TAR	–	–	–	–	–	–	67%	64%
6h window 0.44km N=275	FDR	–	–	–	–	–	–	31%	27%
ECMWF	TAR	–	–	–	–	–	–	81%	73%
12h window 0.44km N=205	FDR	–	–	–	–	–	–	33%	25%
GP	TAR	–	–	–	–	–	–	70%	65%
12h window 0.44km N=205	FDR	–	–	–	–	–	–	24%	20%

against observations taken at Uruguayan meteorological towers. The parameterization utilizes forecasts of resolved-scale (computed on model levels) surface layer conditions, in the form of the Richardson number ( $Ri$ ), the ratio of the vertical stability and vertical wind shear, to predict the  $GF$ , the ratio of the gust and sustained wind. The  $GF$  is then applied to forecasts of sustained wind at wind turbine height (~100 m), yielding gust predictions.

Of particular interest is a parameterization that properly identifies gusty conditions (true alarms) over specified periods (time windows) without offering too many false predictions. Observations indicated that large gusts (exceeding 15 m/s at turbine height) preferentially occurred when the surface layer was near-neutral ( $Ri \sim 0$ ), and that while  $GF$  tended to decrease with sustained wind speed, it was relatively larger

under less stable conditions. These findings were incorporated into the GP, in which a minimum  $GF$  ( $GF_{min}$ ) is adjusted based on the vertical wind variation in the boundary layer above the tower. The intercept  $GF_{min}$  and shear adjustment coefficient  $K$  were permitted to be functions of both sustained wind speed and stability and both were determined using least squares.

The GP was trained against one years' worth of observed and simulated data at the Colonia Eulacio (CE) tower and used to make forecasts for the Rosendo Mendoza (RM) site for the same period. These towers are located in the same region of the country (Fig. 1) but reflect different situations, and our strategy was necessitated in part owing to the quality and quantity of tower data available. Simulations were made using the Weather Research and Forecasting (WRF) model utilizing a variety of

horizontal resolutions and planetary boundary layer (PBL) and surface layer parameterizations. Telescoping nests with grid spacings ranging from 12 km down to 0.444 km were employed, with the finest meshes incorporating both CE and RM tower locations.

Results indicate that our proposed GP can anticipate the occurrence of large gusts, at least within time windows of longer than 1 h. The basic strategy was skillful at separating large from small gust events, but exhibited some bias (underprediction) of the magnitude of large gusts when they did occur, in part because we were employing a model developed for one tower at another. This was remedied via an empirically-determined adjustment factor, dubbed  $S_{Ri}$ . After this adjustment, the GP model was able to identify more than 50% of cases (up to 54%) of large gust events within a 1-h window even when economical (12 km) horizontal resolution forecasts were used (Table 2a). In contrast, the ECMWF formula for non-convective gusts (3) was substantially less successful (event detections  $\leq 41\%$ ), perhaps in part due to the fact it was derived for the 10-m level.

However, for both approaches, this forecast skill came with a large number of false alarms, which motivated the examination of both wider forecast windows and narrower grid spacings. Forecast skill dependence on parameterization also emerged. At still relatively inexpensive 4 km maximum resolution, our GP provided a true alarm rate (TAR) of 69% against a false detection rate (FDR) of 32%, a spread of 37 points, in the 6-h window when the Shin–Höng PBL scheme was used. In the 12-h window, which is useful for staffing and load planning considerations, TAR and FDR with this scheme improved to 70% and 24%, respectively, a 46 point spread. At this grid spacing, the ECMWF algorithm could provide higher TARs, but at the cost of elevated FDRs.

As lower resolution simulations are less expensive, an ensemble of simulations could be made, permitting combinations of gust algorithms and physical parameterizations that can yield more accurate forecasts than a single, deterministic run. Future work can also consider ensemble members employing stochastic perturbations, either to model fields, physics parameters, and/or physics tendencies (Jankov et al., 2017), or more sophisticated data assimilation techniques. In addition, adjustments to account for convectively-driven gusts that might otherwise be missed events have not yet been considered. At this point, however, we have demonstrated that forecast information regarding wind and stability could be used to craft a gust parameterization that can skillfully identify large gusts at reasonable computational expense. Additionally, this research has already provided an electric utility with enhanced wind threat assessments in an area that is very heavily dependent on wind power.

## Acknowledgements

The authors wish to acknowledge the Administración Nacional de Usinas y Trasmisiones Eléctricas (UTE) for providing access to wind and power data; the Cluster FING-UdeLaR and UNIPAMPA for facilitating the development of numerical simulations; the SENAI CIMATEC Supercomputing Center for Industrial Innovation; BG Brazil and the Brazilian Authority for Oil, Gas and Biofuels (ANP) for the provision and operation of computational facilities and for their commitment to invest in Research & Development. RGF was supported by NSF 1450195.

## Appendix A. Supplementary data

Supplementary data related to this article can be found at <https://doi.org/10.1016/j.jweia.2018.04.005>.

## References

Abal, G., D' Angelo, M., Cataldo, J., Gutiérrez, A., 2011. Mapa Solar del Uruguay Version 1.0 Memoria Técnica, first ed. CSIC-UdeLaR, Montevideo.  
 Acevedo, O.C., Fitzjarrald, D.R., 2001. The early evening surface-layer transition: temporal and spatial variability. *J. Atmos. Sci.* 58, 2650–2667.

Ashcroft, J., 1994. The relationship between the gust ratio, terrain roughness, gust duration and the hourly mean wind speed. *J. Wind Eng. Ind. Aerod.* 53, 331–355.  
 Barros, M., 2011. Optimal Control of Wind Turbines in Strong Wind Conditions. Master Thesis. DTU Technical University of Denmark, Department of Mechanical Engineering.  
 Bougeault, P., Lacarrere, P., 1989. Parameterization of orography induced turbulence in a mesobeta-scale model. *Mon. Weather Rev.* 117, 1872–1890.  
 Brasseur, O., 2001. Development and application of a physical approach to estimating wind gusts. *Mon. Weather Rev.* 129, 5–25.  
 Bretherton, C.S., Park, S., 2009. A new moist turbulence parameterization in the Community Atmosphere Model. *J. Clim.* 22, 3422–3448.  
 Brown, D., Reuter, G., 2018. WRF model simulations of the influence of the Athabasca oil sands development on convective storms. *Earth Interact.* 22 (3), 1–25.  
 Cao, Y., Fovell, R.G., 2016. Downslope windstorms of San Diego county. Part I: a case study. *Mon. Weather Rev.* 144, 529–552.  
 Cao, Y., Fovell, R.G., 2018. Downslope windstorms of San Diego County. Part II: physics ensemble analyses and gust forecasting. *Weather Forecast.* 33, 539–559.  
 Chen, F., Dudhia, J., 2001. Coupling an advanced land-surface/hydrology model with the Penn State/NCAR MM5 modeling system. Part I: model description and implementation. *Mon. Weather Rev.* 129, 569–585.  
 Choi, E.C.C., Hidayat, F.A., 2002. Gust factors for thunderstorm and non-thunderstorm winds. *J. Wind Eng. Ind. Aerod.* 90, 1683–1696.  
 Czarnetzki, A.C., 2012. Persistent daytime superadiabatic surface layers observed by a microwave temperature profiler. In: Preprints, 37th Natl. Wea. Assoc. Annual Meeting, Madison, WI, Natl. Wea. Assoc. P2.55.  
 ECMWF, 2015. IFS documentation CY41R1. <https://software.ecmwf.int>.  
 Fernández-González, S., Martin, M., García-Ortega, E., Merino, A., Lorenzana, J., Sánchez, J., Valero, F., Sanz Rodrigo, J., 2018. Sensitivity analysis of WRF model: wind-resource assessment for complex terrain. *J. Appl. Meteor. Climatol.* 57 (3), 477–491.  
 Fovell, R.G., Cao, Y., 2017. The santa Ana winds of southern California: winds, gusts, and the 2016 witch fire. *Wind Struct.* 24, 529–564.  
 Fovell, R.G., Cao, Y., 2014. Wind and gust forecasting in complex terrain. In: Preprints, 15th Annual WRF Users' Workshop, Boulder, CO.  
 Friederichs, P., Gober, M., Bentzien, S., Lenz, A., Krampitz, R., 2009. A probabilistic analysis of wind gusts using extreme value statistics. *Meteorol. Z.* 18, 615–629.  
 Goyette, S., Brasseur, O., Beniston, M., 2003. Application of a new wind gust parameterization: multiscale case studies per formed with the canadian regional climate model. *J. Geophys. Res.* 108 (D13), 4374.  
 Gray, M.E.B., 2003. The use of a cloud resolving model in the development and evaluation of a probabilistic forecasting algorithm for convective gusts. *Meteorol. Appl.* 10, 239–252.  
 Grenier, H., Bretherton, C.S., 2001. A moist PBL parameterization for large-scale models and its application to subtropical cloud-topped marine boundary layers. *Mon. Weather Rev.* 129, 357–377.  
 Gutiérrez, A., Fovell, R.G., 2015. Gust forecasting in Uruguay in support of wind energy. In: 14th International Conference on Wind Engineering Porto Alegre, Brazil.  
 Hansen, A., Cutululis, N., Markou, H., Sørensen, P., Iov, F., 2010. Grid Fault and Design-basis for Wind Turbines. Final report Sørensen, Riso-R-1714(EN).  
 Hong, S., Noh, Y., Dudhia, J., 2006. A new vertical diffusion package with an explicit treatment of entrainment processes. *Mon. Weather Rev.* 134, 2318–2341.  
 IEC. 61400-12, 1998-02. Wind Turbine Generator Systems. Part 12: Wind Turbine Power Performance Testing, first ed.  
 Jankov, I., Berner, J., Beck, J., Jiang, H., Olson, J., Grell, G., Smirnova, T., Benjamin, S., Brown, J., 2017. A performance comparison between multiphysics and stochastic approaches within a North American RAP ensemble. *Mon. Weather Rev.* 145, 1161–1179.  
 Kain, J.S., 2004. The Kain-Fritsch convective parameterization: an update. *J. Appl. Meteor. Climatol.* 43, 170–181.  
 Kain, J.S., Fritsch, J.M., 1990. A one-dimensional entraining/detraining plume model and its application in convective parameterization. *J. Atmos. Sci.* 47, 2784–2802.  
 Kwon, D.K., Kareem, A., Butler, K., 2012. Gust-front loading effects on wind turbine tower systems. *J. Wind Eng. Ind. Aerod.* 104–106, 109–115.  
 Laci, A.A., Hansen, J.E., 1974. A parameterization for the absorption of solar radiation in the earth's atmosphere. *J. Atmos. Sci.* 31, 118–133.  
 Letson, F., Pryor, S.C., Barthelmie, R.J., Hu, W., 2018. Observed gust wind speeds in the coterminous United States, and their relationship to local and regional drivers. *J. Wind Eng. Ind. Aerod.* 173, 199–209.  
 Li, L., Chen, Y., 2017. Numerical simulations of two trapped mountain lee waves downstream of Oahu. *J. Appl. Meteor. Climatol.* 56, 1305–1324.  
 Lin, Y.L., Farley, R.D., Orville, H.D., 1983. Bulk parameterization of the snow field in a cloud model. *J. Clim. Appl. Meteorol.* 22, 1065–1092.  
 Mellor, G.L., Yamada, T., 1974. A hierarchy of turbulence closure models for planetary boundary layers. *J. Atmos. Sci.* 31, 1791–1806.  
 Mellor, G.L., Yamada, T., 1982. Development of a turbulence closure model for geophysical fluid problems. *Rev. Geophys. Space Phys.* 20, 851–875.  
 Mlawer, E.J., Taubman, S.J., Brown, P.D., Iacono, M.J., Clough, S.A., 1997. Radiative transfer for inhomogeneous atmosphere: RRTM, a validated correlated-k model for the long-wave. *J. Geophys. Res.* 102, 16663–16682.  
 Monahan, H.H., Armendariz, M., 1971. Gust factor variations with height and atmospheric stability. *J. Geophys. Res.* 76, 5807–5818.  
 Monin, A.S., Obukhov, A.M., 1954. Basic laws of turbulent mixing in the ground layer of the atmosphere. *Trans. Geophys. Inst Akad. Nauk USSR* 151, 163–187.  
 Nakamura, K., Kershaw, R., Gait, N., 1996. Prediction of near-surface gusts generated by deep convection. *Meteorol. Appl.* 3, 157–167.

- Nakanishi, M., 2001. Improvement of the Mellor-Yamada turbulence closure model based on large-eddy simulation data. *Bound. Layer. Meteor.* 99, 349–378.
- Panofsky, H.A., Tennekes, H., Lenschow, D.H., Wyngaard, J.C., 1977. The characteristics of turbulent velocity components in the surface layer under convective conditions. *Bound. Layer. Meteor.* 11, 355–361.
- Pasquill, F., 1961. The estimation of the dispersion of windborne material. *The. Meteor. Mag.* 90, 33–49.
- Patlakas, P., Drakaki, E., Galanis, G., Spyrou, C., Kallos, G., 2017. Wind gust estimation by combining a numerical weather prediction model and statistical post-processing. *J. Ener. Procedia* 125, 190–198.
- Pleim, J.E., 2007a. A combined local and nonlocal closure model for the atmospheric boundary layer. Part I: model description and testing. *J. Appl. Meteor. Climatol.* 46, 1383–1395.
- Pleim, J.E., 2007b. A combined local and nonlocal closure model for the atmospheric boundary layer. Part II: application and evaluation in a mesoscale meteorological model. *J. Appl. Meteor. Climatol.* 46, 1396–1409.
- Sheridan, P., 2011. Review of Techniques and Research for Gust Forecasting and Parameterisation Forecasting Research Technical Report 570. Exeter, Met Office, UK.
- Shin, H., Hong, S., 2013. Analysis on resolved and parameterized vertical transports in convective boundary layers at gray-zone resolutions. *J. Atmos. Sci.* 70, 3248–3261.
- Shin, H., Hong, S., 2015. Representation of the subgrid-scale turbulent transport in convective boundary layers at gray-zone resolutions. *J. Atmos. Sci.* 143, 250–271.
- Shu, Z.R., Li, Q.S., He, Y.C., He Chan, P.W., 2015. Gust factors for tropical cyclone, monsoon and thunderstorm winds. *J. Wind Eng. Ind. Aerod.* 142, 1–14.
- Siuta, D., West, G., Nipen, T., Stull, R., 2017. Calibrated probabilistic hub-height wind forecasts in complex terrain. *Weather Forecast.* 32, 555–577.
- Skamarock, W.C., 2004. Evaluating mesoscale NWP models using kinetic energy spectra. *Mon. Weather Rev.* 132, 3019–3032.
- Skamarock, W.C., co-authors, 2008. A Description of the Advanced Research WRF Version 3. NCAR/TN 475+STRNCAR Tech. Note.
- Smith, C., Hatchett, B., Kaplan, M., 2017. Characteristics of Sundowner winds near Santa Barbara, CA from a dynamically downscaled climatology. Part I: environment and effects near the surface. *J. Appl. Meteor. Climatol.* (in press).
- Stephens, G.L., 1978. Radiation profiles in extended water clouds. Part II: parameterization schemes. *J. Atmos. Sci.* 35, 2123–2132.
- Stucki, P., Dierer, S., Welker, C., Gomez-Navarro, J.J., Raible, C.C., Martius, O., Brönnimann, S., 2016. Evaluation of downscaled wind speeds and parameterised gusts for recent and historical windstorms in Switzerland. *Tellus* 68, 31820.
- Stull, R.B., 1988. *An Introduction to Boundary Layer Meteorology*, first ed. Kluwer Academic Publishers, Dordrech.
- Takle, E.S., 1983. Climatology of superadiabatic conditions for a rural area. *J. Clim. Appl. Meteorol.* 22, 1129–1132.
- UTE Map of installed power capacity in Uruguay. [www.ute.com.uy](http://www.ute.com.uy) last accessed December of 2017.
- Wieringa, J., 1973. Gust factors over open water and built up country. *Bound. Layer. Meteor.* 3, 424–441.
- WMO Wind gust definition: [www.wmo-sat.info/oscar/variables/view/205](http://www.wmo-sat.info/oscar/variables/view/205), last accessed January of 2018.
- Wyngaard, J.C., 2004. Toward numerical modelling in the Terra incognita. *J. Atmos. Sci.* 61, 1816–1826.